Physica Scripta. Vol. T84, 64–68, 2000

Alfvén Waves, Density Cavities and Electron Acceleration Observed from the FAST Spacecraft

C. C. Chaston, C. W. Carlson, R. E. Ergun and J. P. McFadden

Space Sciences Laboratory, University of California, Berkeley, CA 94720, USA

Received September 6, 1999

PACS Ref: 94.20.Rr

Abstract

Inertial Alfvén waves propagating in regions of auroral electron acceleration are observed from the FAST (Fast Auroral Snapshot) spacecraft over its entire altitude range (350–4180 km). These electron skin depth sized field structures are dispersive and carry an electric field component parallel to the geomagnetic field leading to a variety of non-linear effects including the formation of magnetic field-aligned density cavities and electron acceleration. High resolution measurements show that the electron distribution inside the impulsive wave field envelope or density cavity consists of a cold ionospheric component and an accelerated and heated field-aligned component comprised of downgoing and reflected ionospheric and magnetosheath (solar wind like) electrons. In large amplitude examples the plasma within the wave may be dominated by the accelerated component and the depletion of plasma within the cavity approaches 100%. Comparison of the observed density depletion with the predictions of ponderomotive density cavity formation in association with electron heating shows good agreement. Furthermore, simulations show that most of the observed features of the accelerated component can be explained through Landau resonance of the cold ionospheric and magnetosheath electrons with the inertial Alfvén wave as it propagates through an altitude dependent density profile.

1. Introduction

The presence of Alfvén waves in the auroral oval has been of interest since the pioneering work of [3] who demonstrated their ability in the inertial or kinetic limits [4] to accelerate electrons along geomagnetic field lines into thin curtain like sheets. Since then observations from auroral sounding rockets [5,6] aswell as spacecraft, including S3-3, Freja, Viking and FAST [1,7–10] have shown their prevalence in regions of auroral particle acceleration. It is the purpose of this brief report to describe the plasma environment in which these waves occur and specifically to characterize the plasma observed within the wave field envelope and reconcile these observations with theories of ponderomotive density cavity formation and Landau resonant electron acceleration.

2. The Alfvénic auroral oval

Figure 1 presents a summary of fields and particles data recorded on the FAST spacecraft while traversing the dayside oval at an altitude of 1000 km and passing through a region of strong ELF turbulence. The first two panels show the transverse to $\boldsymbol{B}_0$ electric and magnetic fields with fluctuations amplitudes of up to 500 mV/m and 100 nT indicating E/B ratios of $5.0\times10^6\,\mathrm{ms}^{-1}$. Close inspection of the time series data reveals that this turbulence consists of a series of impulsive 1–2 two cycle fluctuations in both E and B with periods in the range from 0.2 to 0.05 s. The third panel shows that the larger of these fluctuations are accompanied by strong density depletions. These density results have been obtained from the Langmuir probe which has been calibrated for this event by using lower hybrid cutoff in the VLF with the necessary composition data obtained from the plasmaspheric hiss cutoff just below the proton cyclotron frequency Ω_p. The blue trace in this panel is the density as measured by the electrostatic analyser experiment (esa) on board FAST. Of particular interest here is the enhancements seen by the esa and the coincident depletions seen by the Langmuir probe. Since the low energy limit of the esa is $\sim 5\,\mathrm{eV}$ the close agreement of the two different instruments indicates a depletion, or total absence in some cases, of the cold electron population within the Alfvén wave. From the density and composition results the Alfvén speed within the cavities is up to $1.0\times10^7\,\mathrm{ms}^{-1}$ and $2.0\times10^6\,\mathrm{ms}^{-1}$ outside.

The fourth panel shows the field-aligned Poynting flux with positive values indicating downward propagating waves. The green trace is the integrated electron energy flux multiplied by a factor of five for the sake of comparison. It should be noted that these integrated fluxes correspond to a precipitating flux of up to $10\,\mathrm{ergs/(cm^2\,s)}$ at the ionosphere which is well above the $1\,\mathrm{ergs/(cm^2\,s)}$ limit for creating visible aurora [11]. More typically however fluxes are just at or less than this threshold. At times the correlation/anticorrelation between enhanced energy flux and wave Poynting flux is clear. All the integrated electron flux is directed downwards while in general the Poynting flux is mostly downwards but some clear cases of upwards flux are apparent. If the waves are accelerating the electrons then it would appear that the direction of acceleration is independent of the wave propagation direction.

The fifth panel presents the wave electric field spectrum. Throughout the interval the spectrum below Ω_p (black line) is filled with broadband emissions occuring within the wider impulsive fluctuations as has been reported previously by Wahlund *et al.* [8] These waves are oblique with $E_{1\perp}/E_{1||} > 1$ and have a magnetic component satisfying $E_1/B_1 < 10V_\mathrm{A}$ up to frequencies of 50 Hz.

The electron spectra show field-aligned suprathermal electrons with energies of up to a few hundred eV which invariably accompany such intervals of Alfvénic turbulence observed on FAST. As the integrated fluxes and esa density results discussed above suggest, a one to one correlation exists between suprathermal electron bursts and the impulsive Alfvénic E and B fluctuations. The peak in the ion energy spectra at afew hundred eV is a clear signature of magnetosheath ions and appears as isotropic flux outside the loss cone ($130^\mathrm{o} - 230^\mathrm{o}$) in the pitch angle plot. These ions

suggest that FAST remains in the magnetosheric cusp [12] throughout the time when the Alfvénic fluctuations are seen. The broad red line across the bottom of the ion energy spectra is due to the combined effects of ion heating and the apparent energy gain associated with the spacecraft "ramming" ions along its trajectory. These fluxes have been eliminated from the pitch angle plot of the last panel by setting a low energy threshold of 100 eV.

3. "Inside" the Alfvén wave

Figure 2 presents a magnified view of a single impulsive Alfvén wave event. The electric field data shows a sharp boundary at 22:11:55 UT, where the transverse field changes by as much as 500 mV/m, followed by an interval of intense ELF noise with amplitudes of the order of 100 mV/m. The red lines show the filtered electric field for comparison with the DC magnetometer measurements of the next two panels. These curves reveal the waveform of the Alfvén wave with the contribution of higher frequency removed. Amplitudes in B are greater than 100 nT in the west-east direction and less than 50 nT in the north-south direction yielding $E_{\mathrm{N-S}}/B_{\mathrm{W-E}} = 4.0 \times 10^6\ \mathrm{ms}^{-1}$ with V_{A} varying over the interval from 1.0×10^7 down to $2.0 \times 10^6\ \mathrm{ms}^{-1}$.The field variations as seen from the induction coil magnetometer (B_{AC}) show that the much of the higher frequency structure present in the electric field are also present magnetic field fluctuations. These results have been integrated with a full phase/amplitude calibration and accurately represent the magnetic field above 10 Hz. Figure 2(c) indicates how the E/B ratio (normalised to the Alfvén speed) varies with frequency above 10 Hz inside the cavity. Fluctuations below 40 Hz (in the spacecraft frame) have an E/B ratio within a factor of 4 of the Alfvén speed yet above this frequency the wave activity becomes increasingly electrostatic.

The phase difference between the components of E and B varies significantly over the interval leading to a Poynting flux which reverses direction as seen in the seventh panel of Fig. 2(a). However the largest Poynting flux is still directed downwards. The blue line on this panel is the integrated electron flux multiplied by a factor of 5 (as in Fig. 1). Interestingly the peak electron flux is offset from the Poynting flux peak perhaps indicating acceleration at some higher altitude and wave phase. The density results indicated in the seventh panel shows that the Alfvén wave occurs in conjunction within a deep density cavity in which the ELF noise is found. The blue line here is the density obtained from the esa experiment and as noted in the previous section agrees well with the Langmuir probe result within the cavity. Since there is no cold plasma is this cavity the esa experiment sees all the current (except for the small ion current contribution) so that the bottom panel provides an accurate representation of the magnitude and form of the current carried by the Alfvén wave. The magnetometer results show that the current system cannot be an east-west aligned sheet (the classical representation for currents in the aurora) but rather in conjunction with the esa results suggest that the spacecraft passes throught three filamentary upward directed currents with sizes of the order of 1.5 km along the spacecraft track. Less dramatic examples of density cavitation within the wavefield typically show that the energetic population

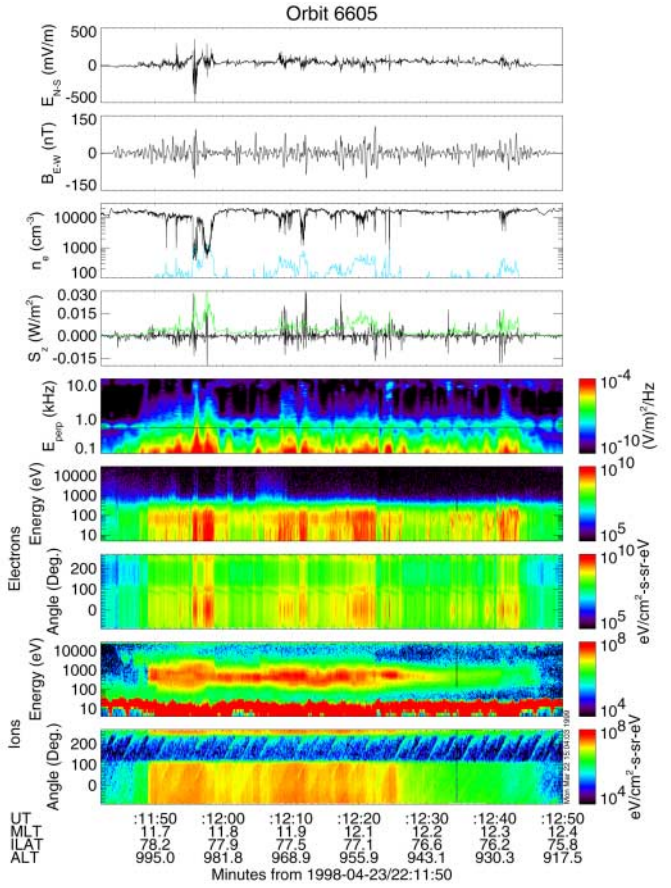

Fig. 1. A FAST cusp crossing. The first panel is the electric field measured along the spacecraft trajectory (or North–South and $\perp \boldsymbol{B}_0$). The second panel is the magnetic field measured by the fluxgate magnetometer instrument in the direction perpendicular to the spacecraft trajectory (or $E-W$ and $\perp \boldsymbol{B}_0$). The third panel shows the electron density measured from the Langmuir probe (black trace) and the electrostatic analyser (esa) experiment (blue trace). The fourth panel is the field-aligned wave Poynting flux (black trace) with positive values corresponding to downwards fluxes. The green line in this panel is the integrated energy flux from the esa multiplied by five. The fifth panel is the spectrum of electric field fluctuations measured $\perp \mathrm{B}_0$ and in the spacecraft spin plane. The remaining panels show the electron and ion energy and pitch angle spectra.

accounts for less than 50% of the total current and less than 10% of the total density.

Figure 2(c) provides a snapshot of the energetic electron distribution captured within the cavity. The dominant feature is the field-aligned (0°) flux below 100 eV most of which falls within the loss cone width which appears to be 100° wide at this altitude (seen in the upper right of the plot). Above 100 eV there is a second field aligned component composed of magnetosheath electrons. The fluxes at energies below 100 eV and angles between 130° and 230° are presumably fluxes of primary and secondary electrons backscattered from the ionosphere. These features will be discussed in more detail in Section 5.

4. Ponderomotive density cavities and electron heating

Several theories concerning density perturbations due to inertial Alfvén waves have been developed [2,13–18]. Careful consideration of the variation in spacecraft potential and the electron saturation current to the Langmuir probes on FAST shows that the measured density depletions are most likely

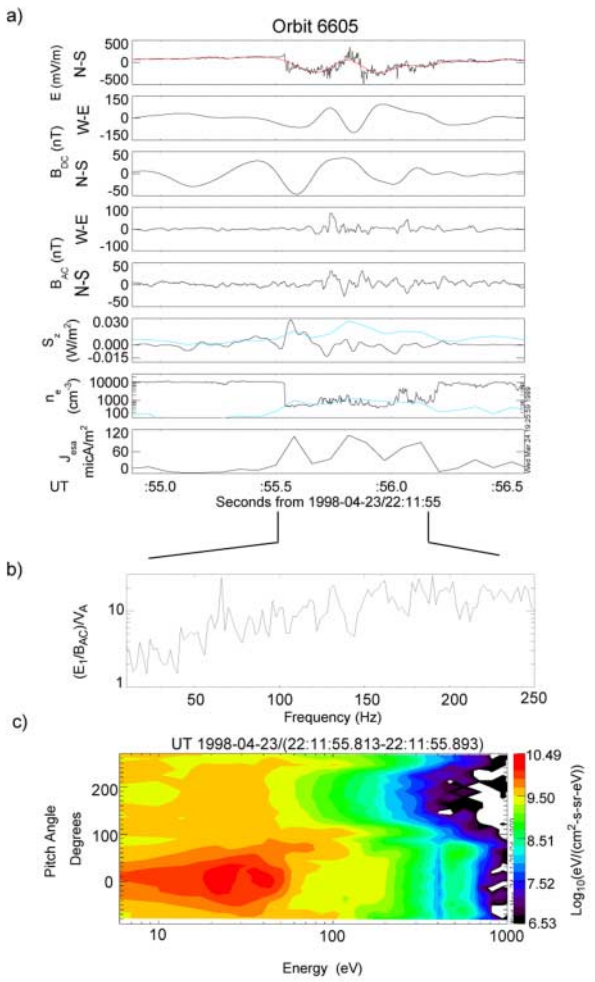

Fig. 2. 'Inside' the Alfvén wave. (a) The first panel show the $\perp \boldsymbol{B}_0$ electric field measured along the spacecraft trajectory (N–S). The red trace is electric field filtered to mimic the fluxgate magnetometer. The third and fourth panels show the DC magnetic field as measured by the fluxgate magnetometer. The fifth and sixth panels are the equivalent integrated AC induction magnetometer results. The seventh panel shows the field-aligned Poynting flux with the integrated electron energy flux (blue trace) multiplied by five. The eigth panel is the langmuir probe density and esa density (blue trace) and the 9th panel is the electron current determined from the ESA experiment. (b) E_1/B_{AC} spectra normalised in terms of the local Alfvén speed (V_{A}). (c) Electron distribution observed coincident with the Alfvén wave.

reliable indications of the true density of the plasma in the Alfvén wave field. Density enhancements are sometimes observed and indeed there may be large variations in Langmuir probe current within a larger density depletion but in general the Alfvén waves observed are coincident with field-aligned density cavities. In this regard [14] and [2] provide easily tested expressions for the expected density depletion associated with the Alfvén wave. The first of these is based on the ponderomotive force created by the oscillating field-aligned current of the Alfvén wave,

$$\Delta n/n_0 = m_{\mathrm{e}}|J_z|^2/4n_0^2e^2\kappa(T_{\mathrm{i}} + T_{\mathrm{e}}) \tag{1}$$

and the second uses the balance between the thermal force due to Joule heating in the Alfvén wave field and the ponderomotive force to produce the expression,

$$\Delta n/n_0 = 1 - \exp\left[-(1 + 8k_\perp^2\lambda_{\mathrm{e}}^2)|\boldsymbol{B}_\perp|^2/48\pi n_0\kappa(T_{\mathrm{i}} + T_{\mathrm{e}}) \times 10^5\right]. \tag{2}$$

Both equations are in SI units where n_0 is the unperturbed plasma density, n is the density inside the cavity, $\Delta n = (n_0 - n)$, m_{e} is the electron mass, e is the electron charge, λ_{e} is the electron skin depth, κ is Boltzmann's constant, T_{i} and T_{e} are the unperturbed ion and electron temperatures in $^\circ K$ and J_z is the field-aligned current density in A/m^2.

Calculation of the field-aligned current during the interval shown in Fig. 1 from the magnetometer measurements and using the assumption of an infinite current sheet, yields current densities of at most 300 μAm^{-2}. Substituition of this current density into Eq. (1) for a background plasma density of 10 000 cm^{-3} from Fig. 1 and ionospheric temperatures $\kappa T_{\mathrm{e}} = \kappa T_{\mathrm{i}} = 0.5$ eV yields $\Delta n/n = 0.05$. Figure 3 shows that this value is well below the observed dn/n (diamonds) values for the 97 events identified in the time series data displayed in Fig. 1. Even if alternate field-aligned current geometries are assumed and κT_{e} is reduced to 0.1 eV the density perturbation still remains below what is observed. So, despite the fact that there may exist a correlation between large gradients in $B_\perp$ and the location of the density cavity [14] the observed cavity depth cannot be explained from this approach.

Results closer to observations are obtained from Eq. (2). The triangles shown in Fig. 3 correspond to the density perturbation calculated using this expression assuming a constant unperturbed plasma density and equal electron and ion temperatures of 10 000 cm^{-3} and 0.75 eV throughout. $k_\perp$ was determined using the assumption of quasi-stationarity of the wavefield over the time it takes the spacecraft to traverse one perpendicular wavelength. The validity of such an approach has been investigated by [10] and we use the statiscal result for the normalised wavenumber obtained from this study of $k_\perp\lambda_{\mathrm{e}} = 0.88$. The trend of observed depletion depth with $\Delta B_\perp$ ($|B_\perp| = 0.5\Delta B_\perp$ in Eq. (2)) seems to track the predicted result with the upper and lower bounds of the distribution fitting closely within reasonable values for ionospheric temperatures and normalised wavenumbers at this altitude.

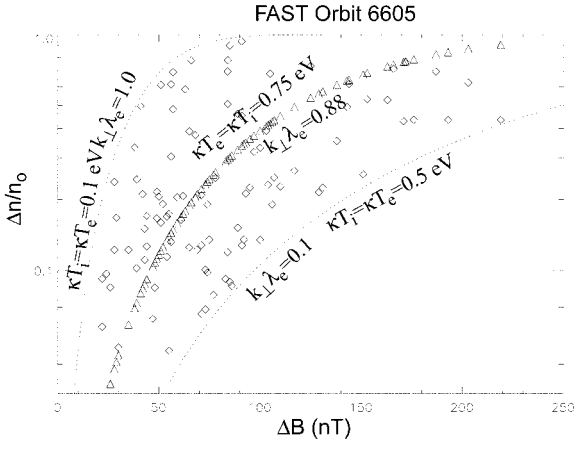

Fig. 3. Scatter plot showing the dependence of density cavity depth ($\Delta n/n_{\mathrm{o}} = (n_{\mathrm{o}} - n)/n_{\mathrm{o}}$) on the magnitude of magnetic field deflection ($\Delta B_\perp$) or Alfvén wave amplitude. Diamond shaped points are the observed results, triangular points are the calculated result from Eq. 2 using $\kappa(T_{\mathrm{i}} + T_{\mathrm{e}}) = 0.75$ eV and the statistical value, $'k'_\perp\lambda_{\mathrm{e}} = 0.88$, and the dashed lines are the calculated results for $\kappa(T_i + T_{\mathrm{e}}) = 0.1$ eV and $k_\perp\lambda_{\mathrm{e}} = 1.0$ (upper limit of data), and $\kappa(T_{\mathrm{i}} + T_{\mathrm{e}}) = 0.5$ eV and $k_\perp\lambda_{\mathrm{e}} = 0.1$ (lower limit of data).

5. Electron acceleration

Perhaps one of the most outstanding features of skin depth sized Alfvén waves in the aurora is their association with suprathermal fluxes of downgoing field-aligned electrons. These accelerated electrons have energies from 10 eV up to 1 keV and sometimes higher on the nightside and may provide precipitating energy fluxes in excess of 10 ergs/cm^2 s. Several theories have been presented to explain the occurence of STEBs associated with Alfvén waves [3,16, 20–23]. Here we present results from a 1-D MHD simulation with an inertial correction for a propagating shear Alfvén wave in a dipole field using a realistic dayside auroral oval density profile. The required equations follow from [22] and are expressed in SI units as,

$$\frac{V_A^2}{c^2+V_A^2}\frac{\partial A_{||}}{\partial z}+\frac{\partial \phi}{\partial t}=0, \tag{3}$$

$$(1+k_\perp^2\lambda_e^2)\frac{\partial A_{||}}{\partial t}+\frac{\partial \phi}{\partial z}=0 \tag{4}$$

where $A_{||}(z,t)$ is the wave vector potential, $\phi(z,t)$ is the wave scalar potential and z is a coordinate representing the altitude with t being time. The relevant boundary conditions are $A_{||}+\mu_0\Sigma_P\phi=0$ at the ionospheric end and $A_{||}+\mu_0\Sigma_A\phi_0(t)=\mu_0\Sigma_A\phi$ at the magnetospheric end which allows the wave to propagate freely out of the model without reflection. Σ_P is the height integrated Pederson conductivity for the ionosphere and $\Sigma_A=1/(\mu_0 V_A\sqrt{1+k_\perp^2\lambda_e^2})$. $\phi_0(t)$ is the applied potential at the magentospheric end required to launch the wave. In the simulation we have used a Gaussian shaped potential with an amplitude of 500 V and a width of 1 s. The perpendicular wavenumber is assumed to scale inversely with the fluxtube width and we take a perpendicular wavelength at the ionospheric end of 500 m with $\Sigma_P=10$ mhos. These values are consistent with the width of observed arcs thought to be associated with inertial Alfvén waves and the expected ionospheric conductivities in the dayside oval. The density profile employed is shown in Fig. 4(a) and follows from observations made from the FAST spacecraft at altitudes from 1000–4000 km, observations from the Polar spacecraft at altitudes above 4000 km [24], and from models [6] at altitudes below 1000 km. The wave is launched from an altitude of 10 000 km and particles injected into the wavefield at various times and altitudes during the simulation. Two types of source distributions are employed, one an ionospheric component modelled as a 2eV isotropic Maxwellian injected at altitudes below 4000 km and the second a magnetosheath like population injected from 10 000 km only and modelled by the downgoing half of a 200 eV isotropic Maxwellian. Figure 4(b) shows a slice taken through the simulation at 2000 km and averaged over 1 second starting just before the Alfvénic pulse reaches that altitude from above. The outstanding feature of the distribution is the downgoing field-aligned component extending from the lowest energy displayed up to one keV. The broad crescent shaped field-aligned feature above 200 eV represents accelerated magnetosheath electrons. Superimposed on the density plot is the wave phase speed given by $V_{\text{inertial}}=\omega/k_{||}=V_A/\sqrt{1+k_\perp^2\lambda_e^2}$ and also the Alfvén speed. Since $E_{||}/E_\perp=(k_{||}k_\perp\lambda_e^2)/(1+k_\perp^2\lambda_e^2)$ the largest parallel fields are found above 3000 km where the inertial correction to Alfvén wave dispersion is largest. Parallel electric field strengths in this region are up to 0.2 mV/m. Consequently, electrons present above 3000 km are accelerated to the largest energies. Energetic magnetosheath electrons entering the simulation from above and travelling with speeds greater than the wave phase speed may overtake the wave and be accelerated to energies of the order of 1 keV as they fall through an essentially static potential drop in the wavefront in the manner discussed by Goertz and Boswell (1979). The majority of electrons (ionospheric) however have thermal velocities along $\boldsymbol{B}_0$ well below the wave phase speed. These particles become resonant with the wave if the upward pointing parallel electric field in the wavefront is large enough to provide acceleration up to the wave phase speed before the field in the electron's frame changes direction. In this way the electrons may be acclerated up to energies of $m_e V_{\text{Inertial}}^2$ as previously discussed by [21]. In this simulation these electrons reach a maximum energy of ~ 600 eV corresponding to twice the inertial Alfvén energy at 3000 km altitude. This maximum energy can be seen as the upper limit of the cold field-aligned beam portion of the simulated distribution shown in Fig. 4(b). Below 3000 km the decreasing Alfvén speed and parallel electric field amplitude mean that fewer electrons are accelerated up to $m_e V_{\text{Inertial}}^2$ and this energy becomes increasing smaller. This effect accounts for the broad energy spread in the

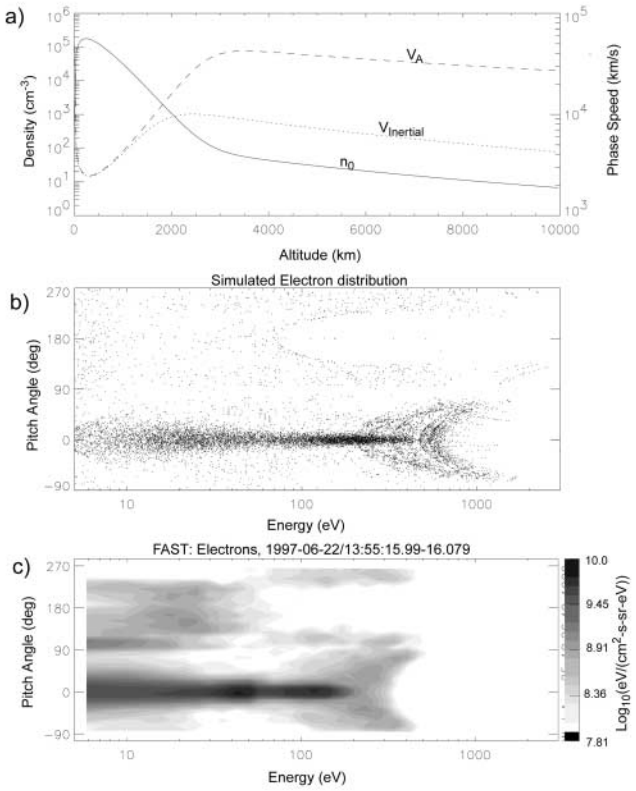

Fig. 4. Electron acceleration; simulation and observations. (a) The altitude dependent density profile used in the simulation and the corresponding Alfvén and inertial Alfvén wave parallel phase speeds assuming a background dipole magnetic field. (b) A pitch angle/energy slice through the simulation at 2000 km and accumulated over 1 s. (c) An observed electron distribution observed coincident with the arrival of an Alfvén wave at 1700 km.

ionospheric portion of the electron beam and tends to diminish energy/time dispersion. In fact, for the density profile and wavenumber choosen, almost no accleration occurs below 2000 km. Between the ionosphere and the 3000 km peak in V_A the Alfvén waves continue to oscillate after the passage of the initial pulse as it reflects between these two boundaries. However, this phase in the simulation provide almost no electron acceleration.

Clearly there are several limitations in this simple model. These include the significant Landau damping (not included) of the wave as it accelerates electrons and the ponderomotive effects on density discussed earlier. Since observations show that the wave Poynting flux is typically an order of magnitude larger than the observed accelerated particle flux the dissipative effects may not be too important for the $k_\perp$ value used here. However, the observations discussed in the previous section do indicate that these waves propagate in density cavities. This allows the wave to have a large parallel electric field component at altitudes well below those modelled here. Consequently, the 'Alfvén resonator' [25] may provide significant electron acceleration. Other short comings relate to the 1-D nature of the simulated Alfvén wave. Observations [26] show that these waves are most likely not periodic in the (North–South) direction (i.e the $k_\perp$ direction) nor infinite in the East–West (where we assume $k_\perp = 0$) direction but are rather localised and often vortical [10]. Finally the simulation has been performed for a H^+–e^- plasma. Addition of O^+ ions particularly at altitudes below 4000 km, where this species may be the dominant ion, significantly reduces the the wave phase speed and magnitude of the parallel electric field and thereby lowers the energy to which electrons may be accelerated.

Despite these limitations the model provides electron distributions which appear similar to observations. Figure 4(c) is an electron distribution observed above the dayside aurora at an altitude of 1700 km. While the maximum energy of the field-aligned component is somewhat less than modelled, its broad energy range with the crescent shaped portion above 100 eV,the widening angular width at lower energies and the loss cone feature at 180° are certainly represented in the simulated result. The enhanced fluxes or electron conics on the edges of the loss cone are also represented in the simulated distribution albeit more particles in the simulation are required to make the result clearer. The largely field-aligned upgoing electrons (120° to 240°) below 100 eV seen in observations are however not represented in the simulation. These electrons are most likely backscattered and secondary electrons from the ionosphere below. Such effects have not been included in the model.

6. Conclusion

In this brief report we have discussed and attempted to explain some of the more physically interesting observations associated with dispersive Alfvén waves in the dayside aurora. Plasma observations within the Alfvén wavefield show a density cavity populated predominately by a cold slowly drifting ionospheric electron component which carries the majority of the field-aligned current and a second accelerated and perhaps heated electron component known as formerly as a STEB (Suprathermal Electron Bursts). It has been shown that the depth of the observed density cavity may well be explained by the ponderomotive force of the Alfvén wave in the presence of electron heating as suggested by [2]. Furthermore, using a simple 1-D model for inertial Alfvén wave propagation in a dipole field and an altitude dependent density gradient it has been shown how the Alfvén wave may provide accelerated electron distributions similar in appearance to those observed through a combination of resonant and effectively static potential drop acceleration mechanisms.

Acknowledgement

This research was funded by NASA under grant NAG-3596

References

1. Carlson, C. W., Pfaff, R. F. and Watzin, J. G., Geophys. Res. Lett. **70**, 2013 (1998).
2. Shukla, P. K. and Stenflo, L., Phys. Plasmas **6**, 1 (1999).
3. Hasegawa, A., J., Geophys. Res. **81**, 5083 (1976).
4. Lysak, R. L. and Lotko, W., J. Geophys. Res. **101**, 5085 (1996).
5. Boehm, M. H., Carlson, C. W., McFadden, J. P., Clemmons, J. H. and Mozer, F. S., J. Geophys. Res. **95, 1990**, 12157 (1990).
6. Knudsen, D. J., M. C. Kelley and J. F. Vickrey, J. Geophys. Res. **97**, 77 (1992).
7. Mozer, F. S. *et al.*, Planet. Space Sci. **38**, 292 (1977).
8. Wahlund, J-E. *et al.*, Geophys. Res. Lett. **21**, 1831 (1994).
9. Aikio, A. T., Blomberg, L. G., Marklund, G. T. and Yamauchi, M., J. Geophys. Res. **101**, 27157 (1996).
10. Chaston, C. C., Carlson, C. W., Peria, W. J., Ergun, R. E. and Mcfadden, J. P., Geophys. Res. Lett. **26**, 647 (1999).
11. Stenbaek-Nielsen, H. C. *et al.*, Geophys. Res. Lett. **25**, 2073 (1998).
12. Heikkila, W. J. and Winningham, J. D., J. Geophys. Res. **76**, 883 (1971).
13. Li, X. and Temerin, M., Geophys. Res. Lett. **20**, 13 (1993).
14. Bellan, P. M. and Stasiewicz, K., Phys. Rev. Lett. **16**, 3523 (1998).
15. Berthomier, M., Pottelette, R. and Treumann, R. A., Phys. Plasmas **6**, 467 (1999).
16. Clark, A. E. and Seyler, C. E., J. Geophys. Res. **104**, 17233 (1999).
17. Shukla, P. K., Stenflo, L. and Bingham, R., Phys. Plasmas **6**, 1677 (1999).
18. Rankin, R., Samson, J. C., Tikhonchuk, V. T. and Voronkov, I., J. Geophys. Res. **104**, 4399 (1999).
19. Goertz, C. and Boswell, R. W., J. Geophys. Res. **84**, 7239 (1979).
20. Temerin, M., McFadden, J. P., Boehm, M., Carlson, C. W. and Lotko, W., J.Geophys. Res. **91**, 5769 (1986).
21. Kletzing, C., J. Geophys. Res. **99**, 11095 (1994).
22. Thompson, B. J. and Lysak, R. L., J. Geophys. Res. **101**, 5359 (1996).
23. Streltsov, A. V. and Lotko, W., J. Geophys. Res. **104**, 4411 (1999).
24. Kletzing, C., Mozer, F. S. and Torbert, R. B., J. Geophys. Res. **103**, 14837 (1998).
25. Lysak, R. L., Geophys. Res. Lett. **25**, 2089 (1998).
26. Volwerk, M. *et al.*, J. Geophys. Res. **101**, 13335 (1996).

